ENGINEER - Vol. LVI, No. 04, pp. [105-119], 2023

https://doi.org/10.4038/engineer.v56i4.7625

Investigation of the Influence of Inner Geometries of the Receiver Tube of a Parabolic Trough Collector System Used for Water Heating

E.M. Ranatunga, N.K. Hettiarachchi, M.K. Abeyratne and M.C.S. Fernando

Abstract: Solar collectors are devices that help to harvest solar thermal radiation and convert into other forms of energy. Because of its low fabrication cost and simple design, the Parabolic Trough Collector (PTC) is one of the finest alternatives for medium-temperature (i.e., in $80°C$-$250°C$ range) needs among all types of concentrated solar collectors. The absorber tube or the receiver tube is one of the main critical components of a PTC. Thermal radiation of the sun falling onto a parabolic reflector is reflected to its focal line where the receiver tube is placed. Therefore, the performance of a PTC system significantly depends on Receiver Geometries (RGs). A locally developed PTC system with a new and accurate tracking system was designed and fabricated in the current study and steam generation inside the receiver was considered in the performance analysis. The experimental analysis was performed using seven different RGs. The experiments were carried out by measuring generated steam every 10 minutes for all the RGs, and simultaneously, solar insolation data was taken by a domestic solar Photovoltaic (PV) system with a capacity of 5 kW. The steam generation data was taken only when the power output of the reference solar PV system was ≥ 4kW. Having tested seven different RGs, the researchers were able to improve the steam generation to a maximum of 10.0% compared to the reference geometry using direct experimental data. This was 8.1% in accordance with the statistical approach via multiple linear regression model. A three-dimensional mathematical model for two-phase flow was formulated for a closed domain. Restricting this model into two-dimensional geometry, the steam generation process was simulated as a TPF problem using ANSYS Fluent software. The volume fraction profiles clearly show the phase transition, which leads to evaporation and condensation inside the tube.

Keywords: Parabolic trough, Solar collector, Receiver, Focal line, Two-phase flow problem

1. Introduction

Solar energy is a resource that is far more abundant and beneficial to the environment than other types of energy sources. This is because the sun emits a significant amount of thermal radiation energy that is transferred to its surroundings in the earth's upper atmosphere. To generate power as efficiently as possible, advanced solar power technology needs to be intensified solar thermal radiation. Electrical and thermal energy requirements can both be met by Concentrated Solar Power (CSP) technology. For CSP technologies, the incoming thermal radiation is focused by mirrors or lenses on a relatively tiny target area, producing medium to high-temperature heat. A high-performance CSP system is achieved as a result of the higher operating temperature, greater heat collection per unit area, and lower absorbing surface area.

Solar concentrators can be categorized into four widely utilized groups, including PTC, Parabolic Dish Collector (PDC), Linear Fresnel Reflector (LFR), and Solar Power Tower (SPT), based on the receiving technology and focus geometry [1]. Here the PTC and LFR are line-focusing CSP systems, while PDC and SPT are point-focusing CSP systems. Again PTC and PDC systems are operated under mobile receivers, while LFR and SPT systems are operated under fixed receivers [2].

Through a numerical analysis, Mhiri et al. [3] investigated the impact of the PTC receiver tube diameter variations. They discovered that

***Mr. E.M. Ranatunga**, B.Sc. (Ruhuna), MPhil. (Ruhuna) PhD. Candidate (Ruhuna), Department of Physics, University of Ruhuna, Sri Lanka.*
***Eng. (Dr.) N.K. Hettiarachchi**, AMIE(SL), B.Sc.Eng. (Hons) (Moratuwa), M.Eng and D.Eng (Kobe University, Japan), Senior Lecturer, Department of Mechanical and Manufacturing Engineering, University of Ruhuna, Sri Lanka.*
***Dr.M.K. Abeyratne,** B.Sc. (Hons) (Kelaniya), PG Dip. In Stat(J'Pura), M.Sc.nat. Dr.rer.nat. (Kaiserslautern, Germany) Senior Lecturer, Department of Mathematics, Faculty of Science, University of Ruhuna, Sri Lanka.*
***Dr. M.C.S.Fernando,** B.Sc. (Hons) (Ruhuna), M.Sc. (Lappeenranta, Finland), Dr.rer.nat. (Kaiserslautern, Germany), Senior Lecturer, Department of Mathematics, Faculty of Science, University of Ruhuna, Sri Lanka.*

improving tube thickness up to a certain level improves the PTC system's performance. Al-Dulaimi et al. [4] have estimated the efficiency of five different shapes of receiver tubes through numerical simulations and theoretical analysis. They concluded that the efficiency of tested receiver shapes could be represented in the following order.

Channel-receiver>Circular-receiver>Square-receiver>Triangular-receiver>Elliptical-receiver.

Liu et al. [5] performed a numerical analysis to determine the thermal performance of a PTC with a ribbed circular receiver. A symmetrical clockwise single inclined receiver, a parallel receiver, a symmetrical counter-clockwise single inclined receiver, a symmetrical counter-clockwise double inclined receiver, and a symmetrical clockwise double inclined receiver are among the five different ribbed receiver tubes that were used in the thermal performance analysis. The findings showed that the symmetrical counter-clockwise double-inclined receiver and the symmetrical clockwise single-inclined receiver provide the highest thermal performance. Concerning the above different outer geometries of receivers, the circular type receiver has been selected in many cases as a significantly better option. However, less effort has been made to develop the inner geometries of receiver tubes.

This study mainly focuses on PTC systems consisting of circular-type receivers. A PTC was designed and fabricated locally and the efficiency was estimated and analyzed under different conditions. Linear focus is produced on a receiver tube along the focal line of a parabola by mirrors, in the shape of a parabolic trough. The parabolic reflector and receiver are mounted on a frame that rotates on one or two axes to track the sun's position throughout the day. The parabolic trough is an optical device in which the reflector's cross-section has the shape of a portion of a parabola. The focal points of the parabolic cross-sections form a focal line in parabolic troughs. Radiation entering a plane parallel to the optical plane is reflected and passed through the focal line. Once the PTC system is fabricated with a selected circular receiver tube, the variations of inner RGs are considered to analyze the performance.

The tracking system is an essential part of CSP systems, and basically, two different methods are used to track the sun, namely, photocell sensor-based tracking systems and astronomical algorithm-based tracking systems (for example, [6], [7] and literature therein). A sun position solar tracking algorithm is a computational method used in solar energy systems to optimize the alignment of solar collectors with the sun's position throughout the day. The algorithm calculates and adjusts the orientation of the solar collectors to ensure that they are always aligned with the sun's position in the sky. This dynamic adjustment maximizes energy production, making solar tracking systems significantly more efficient than fixed installations. Based on a photocell sensor-based tracking system, a novel and modified single-axis Optical Feedback Solar Tracking System (OFSTS) has been introduced as an efficient solar tracking system in this PTC system and a detailed description is given in Section 2.1. For the receiver, seven different inner geometries have been used and analysed.

The process inside the receiver tube is typically modelled as a complicated Two-phase Flow (TPF) problem ([8]-[11]), where the phase transition occurs through evaporation and condensation. We employed the governing equations presented in [8] for this study to explain the interaction of two phases, air and water, using the Volume of Fluid (VOF) technique. Then simulated the problem using a Two-dimensional (2D) RG in ANSYS Fluent to examine the required features such as volume fraction changes, heat distribution, velocity profiles, etc., through the simulated time duration.

Experimentally, the temperature distribution inside the receiver tube was measured every 30 seconds discretely, by using six temperature sensors located at equally spaced points. The amount of steam generation was measured as a distilled water quantity in grams in 10 minute time intervals. In parallel, solar variation was recorded every 5 minutes throughout the period of the experiment.

The Steam Generation Rate (SGR) produced, based on the flux values (SGR/Flux), was calculated experimentally for different RGs and identified the most efficient geometry. To verify the results, a statistical approach was used to estimate the above values for a selected set of experimental data. These experimentally computed values were qualitatively compared with corresponding 2D simulation results.

2. System Design and Fabrication

The experimental PTC system was designed and fabricated with four sub-components: 1) base frame, 2) reflector holder and parabolic reflector, 3) receiver holder and receiver, and 4) tracking mechanism. The base frame structure was fabricated by 25 mm, 50 mm GI box bars with 1.2 mm thickness, each as shown in Figure 1. The reflector holder was fabricated by 25 mm GI box bars of 1.2 mm thickness and two pieces of cladding sheets of size 1.22 m× 0.31 m (thickness = 4 mm). Finally, the cladding sheets were fixed onto the metal structure. The combination of the parabolic reflector and the reflector holder are shown in Figure 2.

The receiver holder and the receiver were designed so that the receiver could be aligned to the focal line of the PTC as much as possible. One can use different techniques, either optical or mechanical, to perform this procedure. However, the receiver tube should be freely adjustable in two directions (along the vertex of the parabola and the perpendicular direction to both vertex of the parabola and the receiver tube). The receiver holder was coupled to the axle and two galvanized plates were mounted just above the receiver tube and these plates were used for fine tracking as an innovative setup (See Figure 3).

Figure 4 shows the tracking mechanism, which consists of 1) stepper motor, 2) gearbox, 3) ball screw, and 4) length variable shaft. The mechanism of the tracking system is discussed in Section 2.1. Two rubber stoppers, two Polly Vinyl Chloride (PVC) reducing sockets, a copper tube (diameter=12 mm, length=1.65m), and a PVC pipe (diameter= 50 mm) were used to fabricate the heat exchanger. The heat exchanger is used to condense the steam and produce distilled water.

A steady water flow was linked to the heat exchanger's water inlet port, and a flexible PVC hose (diameter = 20 mm) was attached to the heat exchanger's water output port. Steam was allowed to flow from the top to the bottom of the copper tube. Hence, the cold water and steam flow inside the receiver were allowed to flow in opposite directions to condense steam effectively and efficiently (See Figure 5). The final experimental setup is shown in Figure 6.

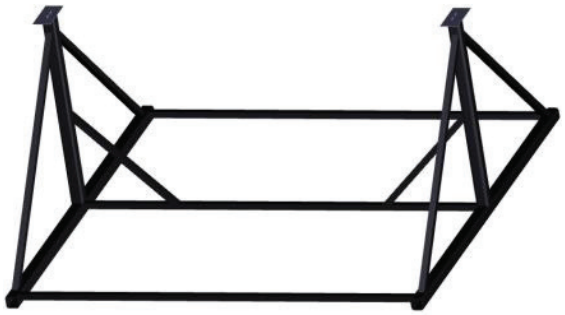

Figure 1 - Base Frame

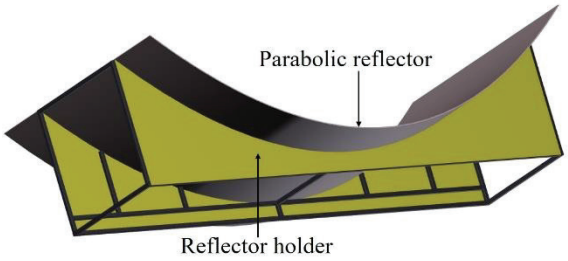

Figure 2 - Reflector and Reflector Holder

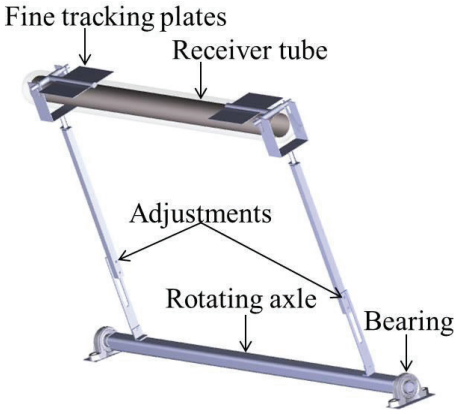

Figure 3 - Receiver Holder

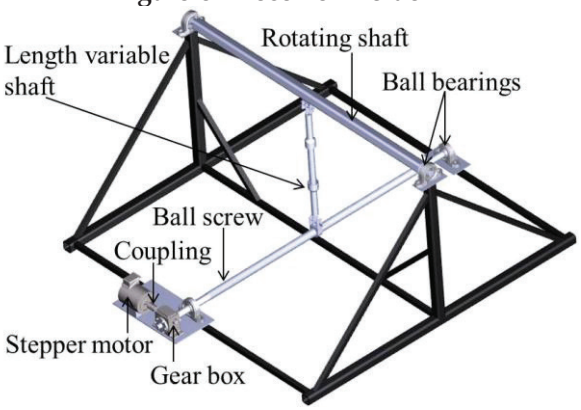

Figure 4 -Tracking Mechanism

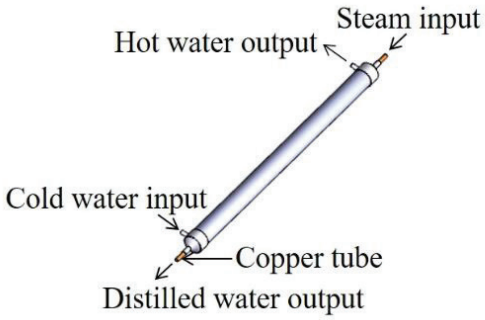

Figure 5 - Heat Exchanger

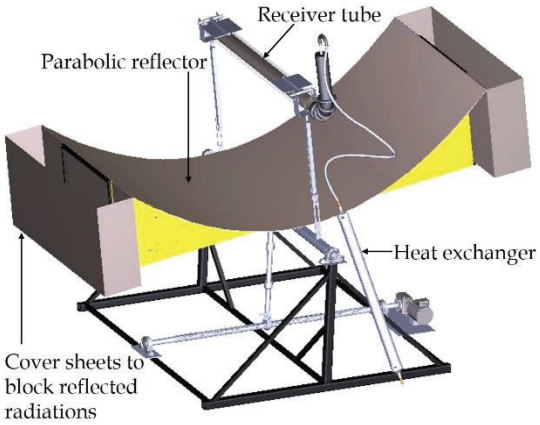

Figure 6 - Final Experimental Setup

2.1 Single-axis OFSTS

CSP systems must be placed in an ideal position perpendicular to the sun's rays during the energy harvesting period to maximize their power output. The installation of a solar tracker is therefore a mandatory requirement for a PTR. A solar tracker is a device to orient CSP systems for concentrating maximum incident light. Compared to a fixed CSP system, a CSP system driven by a solar tracker may boost the energy gain consistently. Several approaches were widely investigated to achieve a higher degree of tracking accuracy in this study and a single-axis optical feedback novel solar tracking system was developed using two BH1750 light sensors controlled by an Arduino board.

BH1750 is a light sensor based on the BH1750FVI intelligent circuit and it is an I2C interfaced digital ambient light sensor [12]. BH1750 IC is appropriate for acquiring ambient light data and a wider range of light intensity can be detected at a better resolution. The digital output value produced by the BH1750 sensor is directly equivalent to the Lux value [12]. Figure 7 shows the BH1750 sensor arrangement in the PTR.

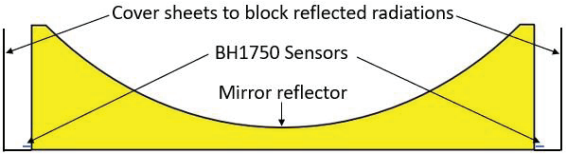

Figure 7 - BH1750 Sensor Arrangement in the PTR

The magnitude of the digital number generated by the BH1750 sensor increases with the intensity of sunlight falling on it. When the PTR is well-tracked, the two light sensors generate approximately equal digital numbers since PTR is symmetrically oriented with the sun. Otherwise, there will be a significant difference in generated numbers depending upon the orientation of the PTR with the sun. Figure 8 shows the well-tracked state of the PTR.

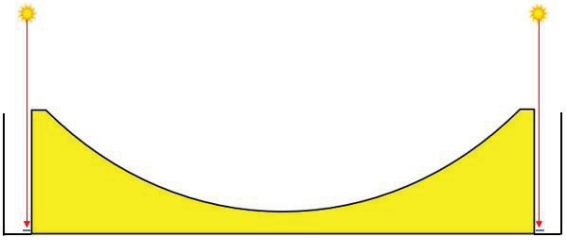

Figure 8 - Well-tracked State of PTR

Then, the Arduino board checks the ratio of two digital numbers generated by BH1750 sensors. The value of the Comparison Number (CN) based on the two digital numbers is defined by Equation 1.

$$CN = \frac{\text{Digital number of left sensor}}{\text{Digital number of right sensor}} \quad \ldots 1$$

At the well-tracked state of the PTR, the value of CN is approximately equal to 1 since the PTR is symmetrical with the sun.

When the condition given in Equation 2 is satisfied, the tracking motor stops rotating. The limiting numbers in Equation 2 were allocated for this novel design, and the value of the ratio of those two digital numbers determines the tracking accuracy of the system. Additionally, the tracking accuracy can be appropriately modified by altering two limiting numbers.

$$0.95 \leq CN \leq 1.05 \quad \ldots 2$$

Figure 9 shows the off-tracked state-1 of PTR with the sun, where the solar radiation falling on the right side < the solar radiation falling on the left side dragging CN below its lower bound. Then, the tracking motor starts rotating clockwise until the CN value resettles within the region specified by Equation 2.

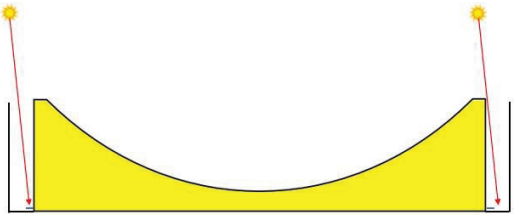

Figure 9 – Off-tracked State of PTR: State-1

Figure 10 shows the off-tracked state-2 of PTR with the sun, where the solar radiation falling on the right side > the solar radiation falling on the left side pushing CN above its upper bound. Then, the tracking motor starts rotating in the counter-clockwise direction until the CN value resettles with the region specified by Equation 2.

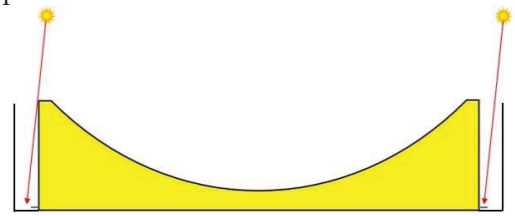

Figure 10 – Off-tracked State of PTR: State-2

The designed single-axis OFSTS was found functioning smoothly and accurately. However, when there is substantial cloud cover, the digital numbers tend to be lower than the given threshold value (which is set at 500), and then the tracking system is set into the standby mode.

2.2 Receiver Geometries of PTR

Although some researchers have conducted studies based on RG in PTR, the optimization of RG is rarely found in literature. Hence, the proposed study concentrates on optimizing the receiver tube geometry to maximize the performance of PTR systems.

Six modified RGs [Receiver Geometry B (RGB), Receiver Geometry C (RGC), Receiver Geometry D (RGD), Receiver Geometry E (RGE), Receiver Geometry F (RGF), and Receiver Geometry G (RGG)] and a Reference Receiver Geometry (RRG) were used in this research. The RRG comprises a single side open evacuated tube used in solar hot water systems whereas the rest of the geometries are modified versions of RRG.

RGB a box bar inserted into RRG

RGC a profile (which divides the receiver volume into three equivalent partitions) inserted into RRG and two upper partitions filled with Nylon profiles as shown in Figure 12

RGD the above mentioned profile inserted into RRG and upper partition filled with Nylon profiles as shown in Figure 13

RGE T-shaped profile inserted into RRG

RGF upside-down T-shaped profile inserted intogeometry A and lower partition filled with Nylon profiles

RGG T-shaped profile inserted into RRG and the upper partition filled with Nylon profiles

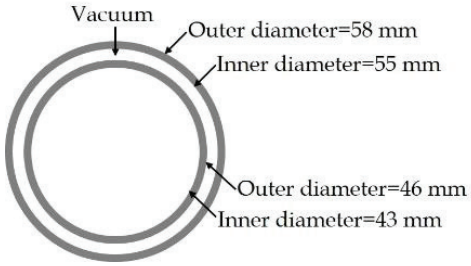

Figure 11 – RRG

RRG, RGB & RGC, RGD & RGE, RGF & RGG are shown in Figure 11, Figure 12, Figure 13 and Figure 14, respectively.

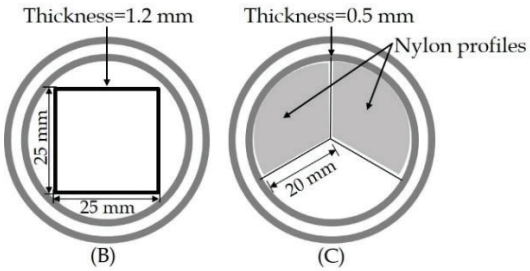

Figure 12–RGB and RGC

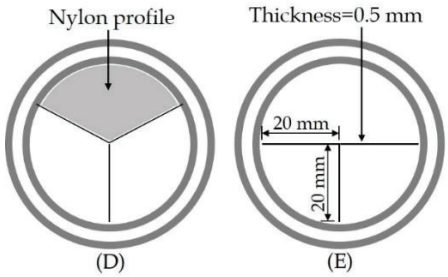

Figure 13 – RGD and RGE

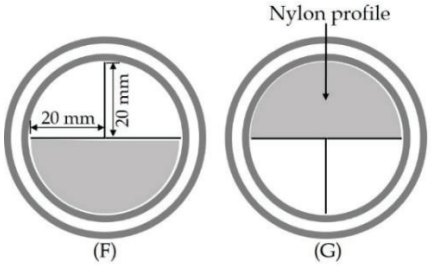

Figure 14 – RGF and RGG

3. Mathematical Modelling

To deliver thermal energy with higher efficiency, a high-performance solar collector is required. Hence, the main key to enhancing PTR efficiency is improving the heat transfer

mechanism inside the receiver tube. A TPF model is presented for the prediction of the characteristics of the TPF of a liquid and its vapor in an angled heat pipe. A 2D mathematical model includes features for calculating the volume fraction and velocity of particles inside the heat pipe. The mathematical model is based on the VOF model used in ANSYS Fluent together with governing equations. The simulation is carried out for a rectangular angled pipe with an open outlet providing a linear heat flux to one of the sidewalls. Typically, the parabolic troughs generated a maximum concentrated heat flux of around 55 kW/m² [13]. We utilized around 45 kW/m² flux to the corresponding wall in this process.

Following assumptions were made for the proposed heat transfer model.

1. A laminar flow of Heat Transfer Fluid (HTF) was considered.
2. Given Boundary Conditions (BCs) are not changing with time.
3. Heat flux is uniform along the receiver tube, but non-uniform concerning the radial direction in Three Dimensional (3D) case.
4. HTF is incompressible.

The volume fraction of each phase in the domain is required to compute the mass, velocity, and temperature profiles in a multi-phase flow. The numerical solutions are finite volume based and are more challenging for multi-phase flows than for single-phase flows. This occurs due to the non-stationary nature of the interfaces between the phases. In such a situation, the physical properties such as density and viscosity fluctuate at the interface.

3.1 Volume of Fluid Method

One crucial parameter in TPF is the volume fraction of a two-phase in a given region. The VOF technique was utilized to tackle these challenges by determining the motion of all phases and indirectly defining the motion of the interfaces [14], [15]. VOF model was proposed by Hirt and Nichols [16], and it can be considered as a simplified technique for solving two-phase problems. Furthermore, the VOF model well satisfies the mass conservation requirements. Using this technique, the volume of the tube can be expressed in terms of the volume of individual phase components. The VOF method can be used for surface tracking on a fixed mesh and is applicable for models involving two immiscible fluids with a well-defined interface between the phases. The VOF model uses a single set of Navier-Stokes equations to track the motion of the various phases by defining the volume fraction of each phase [17]. Each cell in the domain must be filled by one phase or a mixture of the two phases in order to function the VOF model. If the volume fractions of liquid and vapor are$\alpha_l$and α_v, respectively, the following three circumstances are possible:

1. $\alpha_l = 1$: Liquid occupies the entire cell;
2. $\alpha_l = 0$: Vapor occupies the entire cell; and
3. $0 < \alpha_l < 1$: A mixture of liquid and vapor occupies the entire cell.

The volume fractions of all phases add up to 1 when the third criterion is met.

3.2 Governing Equations of Fluid Flow and Heat Transfer

The conservation properties used in the mathematical model are listed as below:

1. The fluid's mass is conserved.
2. The sum of the forces acting on a fluid particle equals the rate of change of momentum.
3. The rate of energy change equals the sum of the rates of heat addition and work performed on a fluid particle.

The continuity, momentum, and energy equations govern heat and mass transfer of a fluid flow. These equations have been considered in the form of standard dimensionless partial differential equations of the Cartesian coordinates. This work uses the ANSYS Fluent code and the VOF method to model the closed TPF system. Song et al. [8] and Fadhl et al. [9] have discussed the VOF model and the Navier-Stokes equations for the VOF model, which are pertinent to our investigation. In the VOF model, the summation of volume fractions of the two-phase must be equal to 1 according to Equation 3.

$$\alpha_l + \alpha_v = 1 \quad \ldots 3$$

Under the following assumptions, Equations 4 and 5 ([8], [18]) represent the continuity equations for vapor and liquid phases, respectively.

1. Phase transition takes place under a constant pressure.
2. Phase transition takes place under a constant temperature.
3. The equilibrium temperature determines the characteristic of mass transfer.

$$\frac{\partial \alpha_l}{\partial t} + \vec{v}.\nabla \alpha_l = -\frac{S_{\alpha_l}}{\rho_l} \quad \ldots 4$$

$$\frac{\partial \alpha_v}{\partial t} + \vec{v}.\nabla \alpha_v = -\frac{S_{\alpha_v}}{\rho_v} \quad \ldots 5$$

Then the momentum equation can be written as Equation 6 ([8], [18], [19]).

$$\frac{\partial}{\partial t}(\rho \vec{v}) + \nabla.(\rho \vec{v}\vec{v}) = -\nabla p + \nabla.[\mu(\nabla \vec{v} + \nabla \vec{v}^{\mathrm{T}})] + \rho g \quad \ldots 6$$

The energy equation can be written in the form of Equation 7 ([8], [19]).

$$\frac{\partial}{\partial t}(\rho h) + \nabla.(\rho \vec{v} h) = \nabla.(\mathrm{k}\nabla \mathrm{T}) + S_E \quad \ldots 7$$

In the VOF model, the enthalpy, h can be written as Equation 8 ([8], [19]).

$$h = \frac{\alpha_l \rho_l h_l + \alpha_v \rho_v h_v}{\alpha_l \rho_l + \alpha_v \rho_v} \quad \ldots 8$$

Since h_l and h_v are based on the specific heat C_l and C_v, respectively, h_l and h_v can be written as Equations 9 and 10, respectively [8].

$$h_l = C_l(T - T_{sat}) \quad \ldots 9$$

$$h_v = C_v(T - T_{sat}) \quad \ldots 10$$

In the TPF, VOF model the ρ, μ and k in each cell can be written as Equations 11, 12 and 13, respectively, [8], [18].

$$\rho = \alpha_l \rho_l + \alpha_v \rho_v \quad \ldots 11$$

$$\mu = \alpha_l \mu_l + \alpha_v \mu_v \quad \ldots 12$$

$$k = \alpha_l k_l + \alpha_v k_v \quad \ldots 13$$

Here ρ, μ and k in Equations 11, 12 and 13 are described as density, viscosity and conductivity in the whole domain.

The two distinct processes of evaporation and condensation are responsible for the heat transfer mechanism. The quantity of heat transfer can be written as the energy equation's source term in Equation 14 [8]. The mass transfers with rate S_a and the amount of energy S_E are released when the phase temperature falls below the equilibrium/saturation temperature T_{sat}. In such situations, those particles try to condense.

$$S_E = S_\alpha \, \Delta H \quad \ldots 14$$

Here the source term is one of the most critical parameters to solve the TPF problem and a proper source term should be substituted to the governing equations to model the liquid-vapor phase change phenomenon [8]. The calculation of mass source terms for the evaporation process and condensation processes given in Equations 15 and 16, respectively, are followed by the studies carried out by Hu et al. [18], [19], [20].

$$S_{\alpha_l} = -S_{\alpha_v} = \beta_1 \alpha_l \rho_l \frac{T - T_{sat}}{T_{sat}}, T > T_{sat} \quad \ldots 15$$

$$S_{\alpha_v} = -S_{\alpha_l} = \beta_2 \alpha_v \rho_v \frac{T_{sat} - T}{T_{sat}}, T < T_{sat} \quad \ldots 16$$

Here the phase transition rate of the vapor and liquid phase is determined by β_1 and β_2, respectively. Here β_1 and β_2 are reference values, which can be considered as tuning parameters. To maintain the saturated temperature at the interface, proper values for β_1 and β_2 described in Equations 15 and 16 should be substituted for relevant source terms.

3.3 Model Geometry and BCs of the 2D Simulation

The TPF model which consists of heat transfer process and other characteristics were simulated and tested using above described model for an angled 2D tube. The corresponding geometry with pre-defined BCs is shown in Figure 15.

Initially, the 2D tube was partly filled (72%) with water. Then the appropriate initial and boundary conditions were applied and the simulation was performed to investigate the bubble generation and steam production inside the tube. More precisely the bottom and left sides of the tube were treated as a diabatic walls, while the right side of the tube was subjected to a constant heat flux as shown in Figure 15.

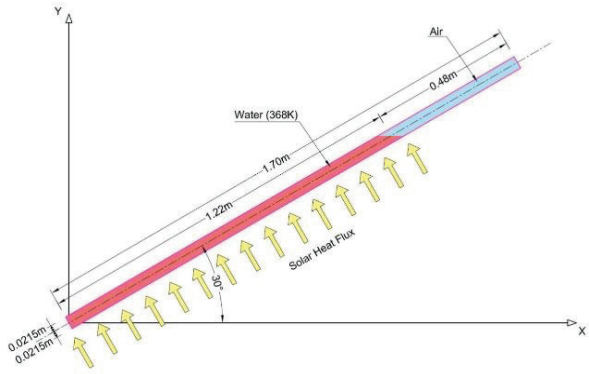

Figure 15 - Model Geometry and BCs

3.4 Computational Mesh of the Simulation

The angle between the horizontal plane and the 2D heat pipe was set as 30° and the computational mesh was constructed (Figure 16) for the simulation according to the model geometry using the ANSYS Fluent software. The grid size of the mesh was set as 0.002 m and respective constant heat flux values were treated in each case at the side wall of the heat pipe as shown in Figure 15. As a BC on adiabatic walls, zero-heat flux was considered. Under the given BCs, the simulation was conducted for 180 seconds of operation. The pressure of the top outlet was considered as the atmospheric pressure.

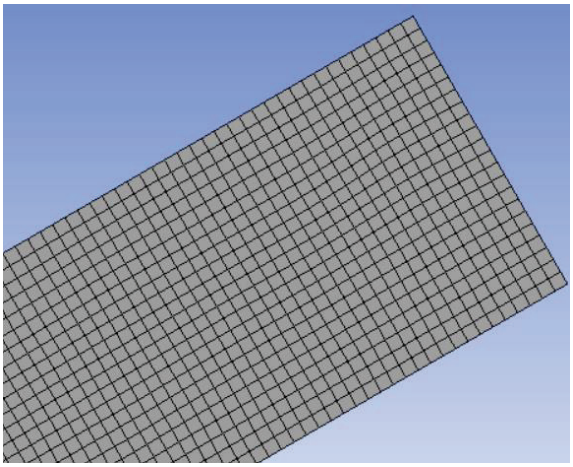

Figure 16 - Part of the Mesh Distribution

4. Experimental Measurements

4.1 Temperature Distribution along the Axis of the Receiver Tube

Six DS18B20 waterproofed digital temperature sensors were used to analyze the temperature distribution along the evacuated tube (RRG). The wires of sensors were covered by flexible PVC hoses and heat sleeves for further waterproofing and protection from high temperatures. An Arduino UNO Rev 3 board was used to carry out the temperature monitoring and recording process. Sensors were linearly placed inside the receiver tube, at a 0.24 m distance, as shown in Figure 17. Then the receiver tube was filled with water and quickly placed on the receiver holder of PTR as data reading should be started before a temperature gradient is generated inside the receiver tube due to solar thermal radiation.

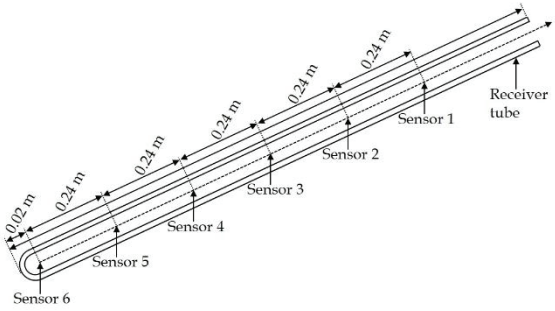

Figure 17 - Temperature Sensor Arrangement inside the Receiver Tube

The temperature of each sensor was recorded in 30 second time intervals under CSP. Data was taken free of cloud cover in the sky as much as possible. The same procedure was repeated under the disturbances of clouds and the PTR was tracked in each case.

4.2 Comparison of SGR of Different RGs

The SID values were recorded every 5 minutes and the steam generation for the bare receiver tube was recorded every 10 minutes. This measurement was conducted in five different experiments under different flux conditions on five different days. The domestic solar PV system is a 5 kW system and the digital number generated in the inbuilt electronic controlling system varies from 0-5000 depending upon the total solar irradiance or solar constant at the location of the solar system and corresponding time. The average value of this digital number in the experimental duration was calculated and the corresponding solar constant was calculated assuming the reference solar constant as1370 Wm^{-2} [21] (i.e., if the solar constant is 1370 Wm^{-2}, digital number is 5000). Hence, calculated solar constant values for Days 1-5 were 1223 Wm^{-2} 1232 Wm^{-2} 1233 Wm^{-2} 1243 Wm^{-2} and 1285 Wm^{-2}, respectively. The flux falling area (A_r) of the receiver tube is given by Equation 17.

$$A_r = 2\pi rl * \frac{2\theta}{360} \quad \ldots 17$$

Here, r, l and θ are receiver diameter, receiver length and rim angle, respectively.

Since,$r = 21.5\,mm$, $l = 1220\,mm$ and $\theta = 80°$, then

$$A_r = 0.073248\ m^2 \quad \ldots 18$$

The effective flux falling area of the mirror is

$$A_m = \text{Trough width} * \text{Trough length} \quad \ldots 19$$

$$\therefore A_m = 2.202 * 1.22 = 2.68644\ m^2 \ldots 20$$

Then the applicable concentrated flux value over the receiver tube for a given solar constant is given by

$$\text{Flux value} = \text{Solar constant} * \left(\frac{A_m}{A_r}\right) \ldots 21$$

SGR merely depends on the corresponding flux value and therefore we considered SGR/Flux value in each case. The flux values, 3D experimental SGR values and SGR/Flux values for the bare tube are shown in Table 1.

The average values of Flux, SGR and SGR/Flux were calculated as shown in Table 1. SGR and corresponding flux values for different RGs were also calculated experimentally as described in Section 4.2. The SGR/Flux values for different RGs are shown in Table 2.

Table 1 - Solar Constant Values and Projected Flux Values for RRG

Day	Flux ($W\,m^{-2}$)	SGR ($g\,s^{-1}$)	(SGR/Flux)/10^{-6} ($g\,s^{-1}W^{-1}m^2$)
1	44855	0.234	5.22
2	45221	0.243	5.37
3	47129	0.275	5.84
4	45588	0.286	6.27
5	45185	0.279	6.17
Avg.	45596	0.263	5.79

Table 2 - Solar Constant Values and Projected Flux Values for Different RGs

RG	Flux (Wm^{-2})	SGR (gs^{-1})	(SGR/Flux)/ 10^{-6} ($gs^{-1}W^{-1}m^2$)
A	45596	0.263	5.79
B	46762	0.258	5.52
C	46762	0.298	6.37
D	46982	0.289	6.15
E	45662	0.247	5.41
F	46028	0.194	4.21
G	45662	0.284	6.22

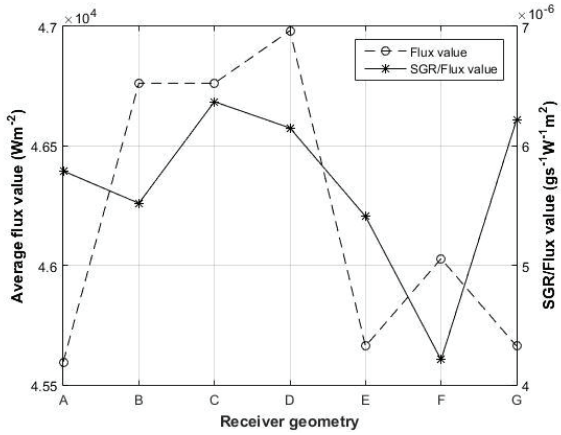

Figure 18 - Average Flux Value and Average SGR/Flux Value for Different RGs

The graphical representation of average Flux value and SGR/Flux value for seven different RGs is shown in Figure 18.

5. Results

5.1 Experimentally Measured Temperature Distribution along the Axis of the Receiver Tube

Figure 19 shows the temperature distribution inside the receiver tube of six different sensors in a low-cloudy environment. Figure 20 shows the same temperature distribution shown in Figure 19 at higher temperatures. According to Figure 19 and Figure 20, there is a significant temperature difference between any adjacent sensors, up to < 95˚C. This happens due to the heated water molecules, which become less dense and move upward. Afterwards, temperature difference between any adjacent sensors was approximately the same since flux distribution along the axis of the receiver tube is the same. However, the temperature sensor placed at the closed end of the receiver tube (Sensor 6) showed an unusual behaviour. But the temperature variation of all other sensors was approximately linear when the temperature was less than 95˚C (see Figure 19).

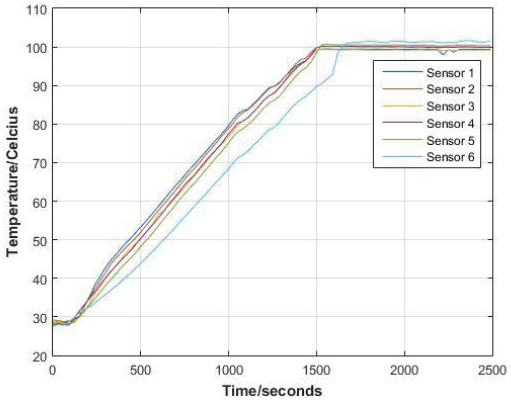

Figure 19 - Temperature Distribution inside the Receiver Tube under a Low Cloudy Environment

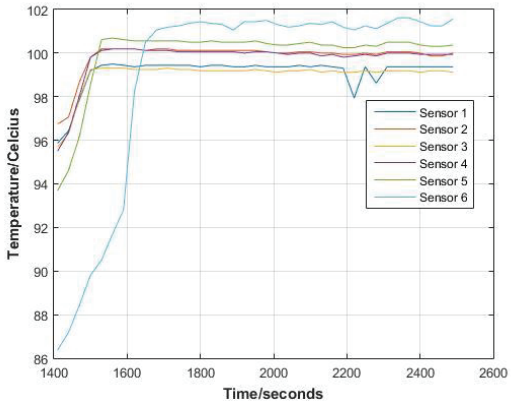

Figure 20 - Temperature Variation at Higher Temperatures under a Low Cloudy Environment

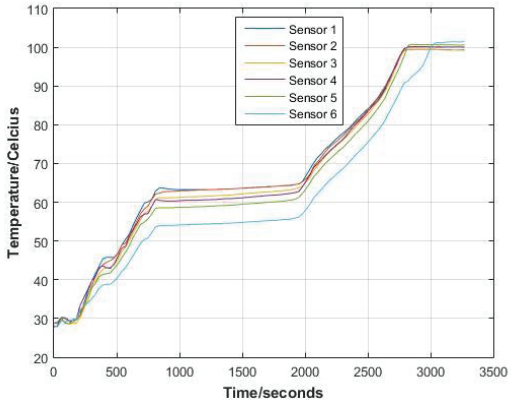

Figure 21 - Temperature Distribution inside the Receiver Tube in a Partially Cloudy Environment

Figure 21 shows the temperature distribution inside the receiver of six different sensors in a partially cloudy environment. According to Figure 21, the presence of cloud covers in the sky while experimenting was clearly indicated on the temperature distribution curves. Furthermore, those cloud cover situations were physically observed and scientifically revealed by Solar Insolation Data (SID) values. A similar pattern of temperature distribution curves was received under the non-concentrated case,

except that it took a long time (~8 times of CSP case) to reach the boiling point.

5.2 Steam-solar Profile for RRG in Different Days

Generally, the Simpson's rule is used to find the estimated value of a definite integral and the basic form of the Simpson's 1/3 rule [22], given by Equation 22.

$$\int_a^b f(x)dx \approx \frac{b-a}{6}\left[f(a) + 4f\left(\frac{a+b}{2}\right) + f(b)\right] \quad ...22$$

As described in Section 4.2, the SID values were recorded every 5 minutes and the steam generation was recorded every 10 minutes. Hence, Simpson's 1/3 rule was used to calculate average solar energy for 10-minute intervals using three adjacent SID measurements. Those calculated values were referred to Sympson's Approximated Solar Power (SASP).

Figures 22-26 show the graphical representations of the variations of SASP and SGR measured on five different days and simultaneous SID values can predict the steam generation curve. Interestingly, steam generation has not fallen with the SID curve at the beginning and end of the day due to the collector tracking the sun. To compensate for that, we may also have to track the solar panels or add some modifications to the data. Alternatively, experimental time could be limited from 11.00 am to 1.00 pm, so that the end effects could be ignored for comparison of various RGs.

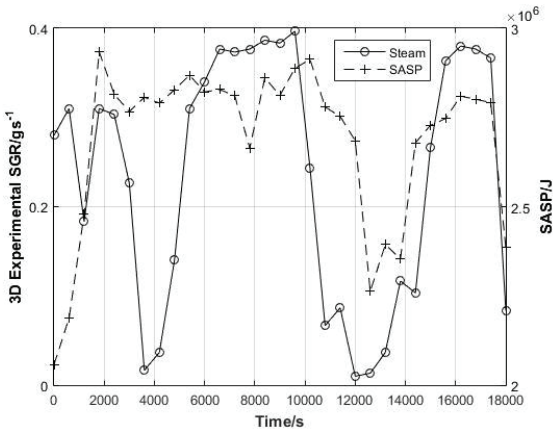

Figure 22 - Variations of SASP and SGR at Day 1

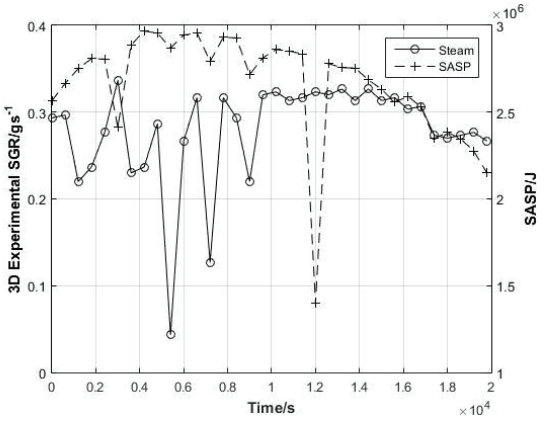

Figure 23 - Variations of SASP and SGR at Day 2

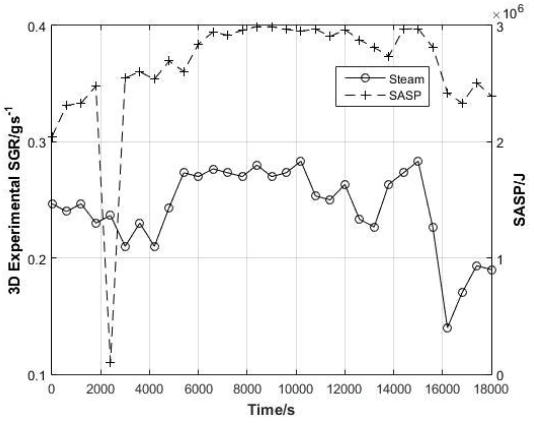

Figure 24 - Variations of SASP and SGR at Day 3

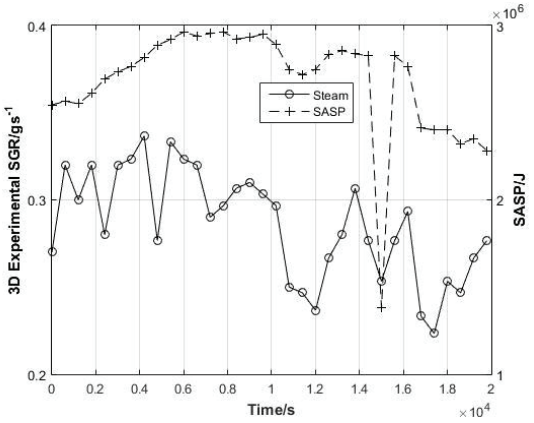

Figure 25 - Variations of SASP and SGR at Day 4

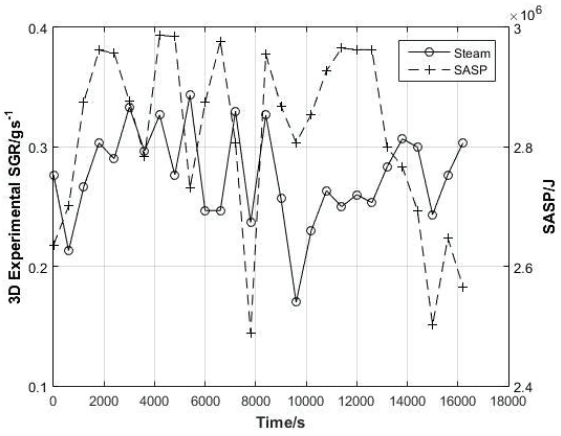

Figure 26 - Variations of SASP and SGR at Day 5

5.3 Experimental Approach for Comparison of RGs

The experimental SGR/Flux values for different RGs are shown in Table 3 and variations of SGR/Flux values in seven different RGs are shown as a bar chart in Figure 27. Figure 27 shows that there are three improved RGs (G, D and C) with respect to RRG. Hence, the order of RGs due to SGR can be represented as F < E < B < A < D < G < C. Hence, the best-improved RG can be concluded as C, which is the three wagons-shaped profile inserted into the bare receiver as shown in Figure 12-(C).

Table 3 - Improvement of SGR/Flux with Respect to RRG

RG	(SGR/Flux)/ 10^{-6} $(gs^{-1}W^{-1}m^2)$	Improvement of SGR/Flux
A	5.79	RRG (0%)
B	5.51	-4.8%
C	6.37	10.0%
D	6.15	6.2%
E	5.41	-6.6%
F	4.21	-27.3%
G	6.22	7.4%

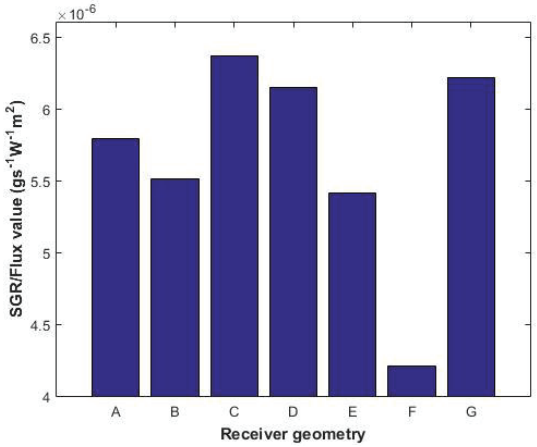

Figure 27 - SGR/Flux Value for Different RGs

5.4 Simulated Results in Ansys FLUENT

Bubble formation and evaporation were observed approximately 23 seconds after the given BCs and with an initial temperature of 368 K, which was physically relevant to the process occurring in solar collector pipes. The tiny bubbles with a lower diameter were generated initially at the flux-applied wall and moved upwards with flow movements. Then tiny bubbles were grouped together, increasing the mean diameter with time. The corresponding volume fraction (of air and water) is provided as a confirmation of the physical relevancy. A higher concentration of vapor is produced as the liquid evaporates. The volume fraction contours corresponding to this boiling phenomenon are illustrated in Figure 28. The simulation results showed that the model utilized is appropriate for understanding the complex phase-change mechanism inside the heat pipe.

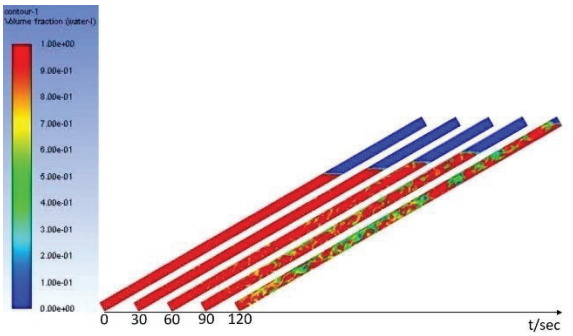

Figure 28 - Contours of Liquid Volume Fraction with Time

5.5 Qualitative Representation of the SGR of 3D Experiment and 2D Simulation Results for RRG

The experimentally measured SGR values were calculated in five cases for RRG. Then five corresponding 2D simulations were carried out to find out the SGR values numerically with the respective flux values in the experimental case. The Average Flux Values (AFV), the experimental SGR values, the Numerical SGR (NSGR) values and the corresponding SGR/Flux values for the two cases are shown in Table 4.

Table 4 - Calculated SGR by Experimentally and Numerically

AFV ($W m^{-2}$)	NSGR (2D) (gs^{-1})	(SGR/Flux)/10^{-6} ($gs^{-1}W^{-1}m^2$)	
		3D Exp.	2D Num.
44855	0.010154	5.22	0.2264
45185	0.010392	6.17	0.2300
45221	0.010418	5.37	0.2304
45588	0.010667	6.27	0.2340
47129	0.011547	5.84	0.2450

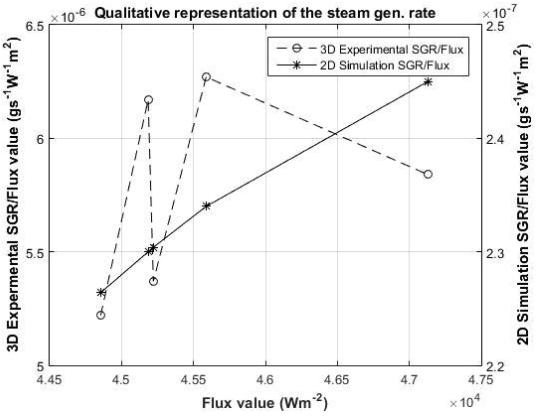

Figure 29 - Qualitative Representation of the SGR/Flux of Experimental and Simulation Results for RRG

According to Table 4, qualitative representation of the SGR of experimental and simulation results are shown in Figure 29. Here we compared SGR/Flux values of 2D numerical simulation and 3D experimental case. Therefore, the comparison may not be that much accurate for fully quantitative analysis. This problem can be overcome by upgrading the numerical simulation into dimension three.

5.6 Statistical Approach for Comparison of the Performance of RGs using Experimental Data

Regression analysis is a statistical technique used to investigate correlations between variables. Multiple linear regression is a generalization of simple linear regression, which is used to evaluate the linear relationship between a quantitative response variable and several predictor variables [23].

After confirming the required assumptions, such as normally distributed solar energy patterns, a multiple regression model was fitted to predict the amount of steam production by considering solar power and receiver geometries (referred as (RG) 1-7) as predictor variables. The equation of the fitted model is given by Equation 23. The term solar in Equation 23 represents the SASP (Solar power for 10 minutes).

$$\begin{aligned} \text{Steam} &= -153.4 \\ &+ 0.0001181 * Solar \\ &- 2.607 * RG2 \\ &+ 10.91 * RG3 \\ &+ 3.998 * RG4 \\ &- 2.827 * RG5 \\ &- 1.852 * RG6 \\ &- 4.253 * RG7 \end{aligned} \quad \ldots 23$$

Equation 23 can calculate the amount of steam generation (in grams) for the duration of 10 minutes. For example, if we want to calculate the steam generation for $RG2$ for a given solar value (Assume 2700 kJ), then we must substitute $RG2 = 1, RG3 = RG4 = RG5 = RG6 = RG7 = 0,$ in Equation 23. Hence, the amount of generated steam for 10 minutes in RG2 is given in Equation 24.

$$\begin{aligned} \text{Steam}_{MC2} &= -153.4 \\ &+ 0.0001181 * 2700000 \\ &- 2.607 = 162.863\ g \end{aligned} \quad \ldots 24$$

Then the SGR for RG2 per second can be calculated as stated in Equation 25.

$$SGR_{MC2} = \frac{162.863}{600} = 0.271 gs^{-1} \quad \ldots 25$$

Based on Equations 23, 24 and 25, SGR and SGR/Flux values for all other RGs are shown in Table 5. The percentage improvement of SGR/Flux with respect to RRG is shown in Table 6. The bar graph of the SGR/Flux value for different RGs for a given solar value (2700 kJ) is shown in Figure 30, according to Table 6.

Table 5 – SGR and SGR/Flux for Different Receiver Geometries

RG	Flux (Wm^{-2})	SGR (gs^{-1})	(SGR/Flux)/10^{-6} ($gs^{-1}W^{-1}m^2$)
1	45576	0.276	6.06
2	44767	0.271	6.05
3	44854	0.294	6.55
4	44189	0.282	6.38
5	43911	0.271	6.17
6	45041	0.273	6.06
7	44405	0.269	6.06

Table 6 - Statistical Percentage Improvement of SGR/Flux with respect to RRG

RG	(SGR/Flux)/10^{-6} ($gs^{-1}W^{-1}m^2$)	Percentage improvement
1	6.06	RRG (0%)
2	6.05	-0.2%
3	6.55	8.1%
4	6.38	5.3%
5	6.17	1.8%
6	6.06	0%
7	6.06	0%

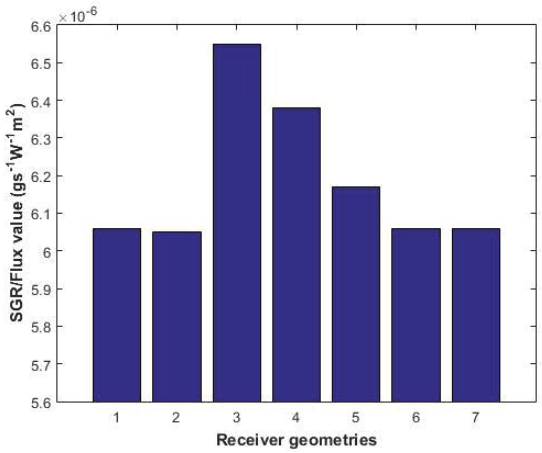

Figure 30 – SGR/Flux Value for Different Receiver Geometries

Hence, the order of receiver geometries due to SGR can be represented as RG1=RG2=RG6=RG7<RG5<RG4<RG3.

Hence, the best receiver geometry can be concluded as RG3, which is the three wagons-shaped profile inserted into the reference receiver as shown in Figure 12-(C).

Based on the adjusted R-squared value of the fitted model, 72.13% variation of the response variable, steam, can be explained by solar power and seven different receiver geometries. There is a significant and positive relationship between steam and solar power. So, for an increase of one unit in solar power, steam increases, on average, by 0.0001181, for a constant level of all the other receiver geometries. Here, the RG1 is used as the reference variable, and the variations of the amount of the steam produced by other receiver geometries are explained concerning RG1.

Based on Table 3 and Table 6, both the experimental approach and statistical approach yielded relatively close percentage improvements for SGR/Flux which were 10.4% and 8.1%, respectively.

6. Conclusions

In this research project, we introduced a novel solar tracking system based on an optical feedback method. This tracking system is enriched with the following advantages.

1. Since two light sensors are placed at a significant distance, i.e., 2.44 m apart, it gains a higher accuracy.
2. The capability of adjusting the tracking accuracy appropriately by changing the upper and lower bounds of CN.
3. Capability of extending the solar tracking system as a dual-axis tracking system, using four light sensors.
4. Possibility of fine-tuning the tracking mechanism by changing the threshold value.

Estimating the temperature distribution profile inside the receiver tube is a significant finding since one can perceive what is physically happening inside the receiver tube. Although there was a temperature gradient along the axial direction of the receiver at the beginning of the experiment, ultimately the whole domain reached approximately an equal temperature (near the boiling temperature). However, using a double-side opened tube would enhance the steam generation efficiency, since the continuous water input to the receiver tube does not drop the temperature at the steam-generating surface.

The results of the Computational Fluid Dynamics (CFD) simulations indicate that the employed model successfully reproduces the complex phenomena of the TPF system. Further improvements over more comprehensive operating ranges are still required for the suggested CFD model, which should be tested using the experimental data. In the simulation, the bubble formation and evaporation were seen under the given BCs, which were physically relevant to the process occurring in solar collector pipes. The bubbles were generated at the flux-applied wall and moved upwards with flow movements. The corresponding volume fraction (of air and water) profile is provided as a confirmation of the physical relevancy.

The incoming heat flux warms the angle pipe, causing the creation of bubbles at the beginning of the heating-up process. Mainly tiny bubbles having a lower diameter were generated near the flux-applying wall and then tiny bubbles were grouped together, increasing the mean bubble diameter with time. The evaporation of a liquid results in a rise in the vapor content and, consequently, the volume fraction of vapor. According to the simulation results, CFD can be useful for understanding the complex phase-change process inside the heat pipe. The results agreed with phase transition, leading to evaporation and condensation inside the pipe.

The simulation results of the 2D model are helpful for improving the outer shapes of the receiver tube, like its diameter and length.

Additionally, experimenting with different inner shapes of the receiver tube gives us more choices to enhance the system. By combining these two approaches, we can create one of the most efficient systems by optimizing both the outer and inner geometries of the receiver tube. Optimization of the inner geometries is one of the leading research outcomes of the experimental results that can be quantified explicitly with a linear regression model. Having tested seven different RGs, it was able to improve the SGR/Flux to a maximum of 10.0% compared to RRG using direct experimental data. This was 8.1% in accordance with the statistical approach via multiple linear regression model. Obtaining 3D simulation results for the actual geometry using the mathematical model described above would be a challenging task. Alternatively, using different types of outer geometries of the receiver tube, such as square, rectangle, etc., the 2D simulation results can easily be projected into the experimental setup for a better validation. Nevertheless, such considerations can be addressed as a further investigation.

Nomenclature/Abbreviations

PTC	Parabolic Trough Collector
RG	Receiver Geometry
PV	Photo Voltaic
CSP	Concentrated Solar Power
PDC	Parabolic Dish Collector
LFR	Linear Fresnel Reflector
SPT	Solar Power Tower
OFSTS	Optical Feedback Solar Tracking System
TPF	Two-Phase Flow
VOF	Volume of Fluid
SGR	Steam Generation Rate
2D	Two Dimensional
PVC	Polly Vinyl Chloride
CN	Comparison Number
RRG	Reference Receiver Geometry
RRB	Reference Receiver B
RRC	Reference Receiver C
RRD	Reference Receiver D
RRE	Reference Receiver E
RRF	Reference Receiver F
RRG	Reference Receiver G
HTF	Heat Transfer Fluid
BC	Boundary Condition
3D	Three Dimensional
SID	Solar Insolation Data
SASP	Sympson's Approximated Solar Power
AFV	Average Flux Value
NSGR	Numerical SGR
CFD	Computational Fluid Dynamics

Acknowledgement

This research was funded by the grant PG2017(I)/RUH/02 of the University Grant Commission (UGC), Sri Lanka. Authors acknowledge the support extended by Mr. Wasantha Abeygoonarathna, Chairman of Highray Engineering.

References

1. Islam, R., Bhuiyan, A. B. M. N., and Ullah, W., "An Overview of Concentrated Solar Power (CSP) Technologies and its Opportunities in Bangladesh," No. February, 2017, doi: 10.1109/ECACE.2017.7913020.

2. Power, C. S., "Csp_roadmap.pdf," *Int. Energy Agency*, pp. 11–12, 2010, [Online]. Available: https://iea.blob.core.windows.net/assets/663fabad-397e-4518-802f-f1c94bc2076/csp_roadmap.pdf.

3. Ghomrassi, A., Mhiri, H., and Bournot, P., "Numerical Study and Optimization of Parabolic Trough Solar Collector Receiver Tube," *J. Sol. Energy Eng. Trans. ASME*, Vol. 137, No. 5, pp. 1–10, 2015, doi: 10.1115/1.4030849.

4. Al-Dulaimi, M. J., and Amori, K. E., "Effect of Receiver Geometry on the Optical and Thermal Performance of a Parabolic Trough Collector," *Heat Transf.*, Vol. 51, No. 3, pp. 2437–2457, 2022, doi: 10.1002/htj.22406.

5. Liu, P., Lv, J., Shan, F., Liu, Z., and Liu, W., "Effects of Rib Arrangements on the Performance of a Parabolic Trough Receiver with Ribbed Absorber Tube," *Appl. Therm. Eng.*, Vol. 156, No. January, pp. 1–13, 2019, doi: 10.1016/j.applthermaleng.2019.04.037.

6. Nwanyanwu, C. J., Dioha, M. O., and Sholanke, O. S., "Design, Construction and Test of a Solar Tracking System Using Photo Sensor," Vol. 6, No. 03, pp. 169–175, 2017.

7. Rizal, Y., and Hasta, S., "Application of Solar Position Algorithm for Sun-tracking System," *Phys. Procedia*, Vol. 32, pp. 160–165, 2013, doi: 10.1016/j.egypro.2013.05.021.

8. Song, H., Zhang, W., Li, Y., Yang, Z., and Ming, A., "Simulation of the Vapor-liquid Two-phase Flow of Evaporation and Condensation," *Int. J. Heat Technol.*, Vol. 34, No. 4, pp. 663–670, 2016, doi: 10.18280/ijht.340416.

9. Fadhl, B., Wrobel, L. C., and Jouhara, H., "Numerical Modelling of the Temperature Distribution in a Two-phase Closed Thermosyphon," *Appl. Therm. Eng.*, Vol. 60, No. 1–2, pp. 122–131, 2013, doi: 10.1016/j.applthermaleng.2013.06.044.

10. Lenhard, R., Malcho, M., and Jandačka, J., "Modelling of Heat Transfer in the Evaporator and Condenser of the Working Fluid in the Heat," Vol. 7632, 2018, doi: 10.1080/01457632.2018.1426225.

11. Fadhl, B., Wrobel, L. C., and Jouhara, H., "Modelling of the Thermal Behaviour of Heat Pipes," Vol. 83, pp. 377–389, doi: 10.2495/HT140331.

12. Gao, J., Luo, J., Xu, A., and Yu, J., "Light Intensity Intelligent Control System Research and Design Based on Automobile Sun Visor of BH1750," *Proc. 29th Chinese Control Decis. Conf. CCDC 2017*, pp. 3957–3960, 2017, doi: 10.1109/CCDC.2017.7979192.

13. Wu, Z., Li, S., Yuan, G., Lei, D., and Wang, Z., "Three-dimensional Numerical Study of Heat Transfer Characteristics of Parabolic Trough Receiver," *Appl. Energy*, Vol. 113, pp. 902–911, 2014, doi: 10.1016/j.apenergy.2013.07.050.

14. De Schepper, S. C. K., Heynderickx, G. J., and Marin, G. B., "Modeling the Evaporation of a Hydrocarbon Feedstock in the Convection Section of a Steam Cracker," *Comput. Chem. Eng.*, Vol. 33, No. 1, pp. 122–132, 2009, doi: 10.1016/j.compchemeng.2008.07.013.

15. Canonsburg, T. D., "ANSYS Fluent Theory Guide," *ANSYS Inc., USA*, Vol. 15317, No. November, p. 814, 2013, [Online]. Available: http://www.afs.enea.it/project/neptunius/docs/fluent/html/th/main_pre.htm.

16. Hirt, B. D. N. C. W., "Volume of Fluid (VOF) Method for the Dynamics of free Boundary," *Iran. J. Sci. Technol. - Trans. Electr. Eng.*, Vol. 42, No. 3, pp. 357–366, 2018, doi: 10.1007/s40998-018-0069-1.

17. Alvarez Ortiz, J., Salinas, J., and Romero Domínguez, R., *Introducción al Estudio Fluido Dinámico de la Uretra.*, Vol. 7, No. 5. 1983.

18. Yang, Z., Peng, X. F., and Ye, P., "Numerical and Experimental Investigation of Two-phase Flow During Boiling in a Coiled Tube," Vol. 51, pp. 1003–1016, 2008, doi: 10.1016/j.ijheatmasstransfer.2007.05.025.

19. Sun, D., "Modeling of the Evaporation and Condensation Phase-change Problems with FLUENT," No. March, 2015, doi: 10.1080/10407790.2014.915681.

20. Channels, P., "Numerical Investigation on Two-phase Flow Heat Transfer Parallel Channels," 2021.

21. Wald, L., and Basics, L. W., "Basics in Solar Radiation at Earth Surface-Revised Version #2," No. July, pp. 7–8, 2019, [Online]. Available: https://hal.archives-ouvertes.fr/hal-02175988.

22. Andrew, A. M., "Homogenising Simpson's Rule," Vol. 31, No. 2, pp. 282–291, doi: 10.1108/03684920210417328.

23. Tranmer, M., Murphy, J., Elliot, M., and Pampaka, M., "Multiple Linear Regression (2 nd Edition) Mark Tranmer Maria Pampaka January 2020 License and Attribution," No. January, pp. 1–59, 2020, [Online]. Available:https://hummedia.manchester.ac.uk/institutes/cmist/a rchive-publications/working-papers/2020/2020-1-multiple-linear-regression.pdf.